Journal of Magnetism and Magnetic Materials 590 (2024) 171656

Contents lists available at ScienceDirect

Journal of Magnetism and Magnetic Materials

journal homepage: www.elsevier.com/locate/jmmm

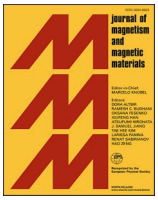

Optimized $Mn_{0.5}Zn_{0.5}Fe_2O_4$ nanoflowers based magnetic fluids for potential biomedical applications

Hima Patel [a], R.V. Upadhyay [a], Kinnari Parekh [a,*], Dennys Reis [b], Cristiano L.P. Oliveira [b], A.M. Figueiredo Neto [b]

[a] Dr. K C Patel R&D Centre, Charotar University of Science and Technology, CHARUSAT campus, Changa 388 421, Gujarat, India
[b] Instituto de Fisica, Universidade de Sao Paulo, R. do Matão, 1371 - Butantã, São Paulo, SP 05508-090, Brazil

ARTICLE INFO

Keywords:
Nanoclusters
Magnetic particles
U/SAXS
Hydrothermal route
Magnetic fluid hyperthermia
Core-shell structure

ABSTRACT

Magnetic nanoclusters of the nanoflower type exhibit unique physical and magnetic properties as compared to their constituent nanoparticles due to the intra-cluster interactions. The present work highlights the maneuvering of $Mn_{0.5}Zn_{0.5}Fe_2O_4$ nanoflower-based magnetic fluids for possible biomedical applications. The formation mechanism of the nanoflowers and the strategies to control the dimensions of the nanoflowers are described in detail. The nanoflowers are characterized using different structural and magnetic techniques: XRD, TEM, DLS, U/SAXS, BET, VSM, and induction heating. The size of nanoflowers is tuned from 107 to 218 nm using the hydrothermal route by controlling the reaction time. The core–shell cluster model is developed to fit the SAXS data to retrieve the size of the nanoflowers as well as their constituent particles. It is seen that the cluster sizes obtained from various techniques are complementary to each other. This is a first attempt of its kind to show that the size of nanoclusters determined by different techniques (TEM, DLS, and U/SAXS) are comparable. Also, the size and size distribution of constituent particles within a cluster/flower complement each other (XRD, TEM, U/SAXS and Magnetization). The results are explained using the surface area and porosity of nanoflowers determined using the BET technique. The dispersion of nanoflowers can be used for magnetic fluid hyperthermia as well as for other applications where a large surface area-to-volume ratio is desirable.

1. Introduction

Magnetic fluid hyperthermia (MFH) has attracted researchers around the world to safely kill cancer cells using the heat generated by magnetic nanoparticles under a high-frequency alternating magnetic field [1]. The heating efficiency of the magnetic materials depends on various parameters such as chemical composition, size, shape, and size distribution of the particles, their saturation magnetization, dispersion stability, etc. [2]. The uniformity in size and shape of magnetic nanoparticles greatly affects the effectiveness of the results. Moreover, the size and shape of the particles also play a crucial role in enhancing the induction heating property, as it is mainly dominated by the Brownian relaxation mechanism of the magnetic nanoparticles. It is reported that the monodispersed sample with 0.10 polydispersity has around twice (700 K/s) as much induction heating as broad polydispersive samples (350 K/s for 0.25 polydispersity) [2,3]. At the same time, over different shapes of particles (such as cubes, disks, spindles, and nanoclusters), it is reported that magnetic nanoclusters (also known as multi-core nanocrystals) exhibit a maximum specific absorption rate (SAR) over other shapes of particles [4]. The nanoclusters consist of several small-sized particles along with voids inside the structure. Within a nanocluster, the small particles are arranged themselves so that the nanoclusters become energetically stable. The magnetic properties of such nanoclusters are, thus, a function of size, number density, and distance between the particles within a nanocluster.

The synthesis of magnetic nanoclusters of 85 nm in typical size with a narrow size distribution was reported by Liu et al. [5]. Damodaran et al. [6] reported the synthesis of magnetic nanoclusters of 120 nm, consisting of a large number of individual magnetic nanoparticles (<10 nm). The parameters used to tune the size of the nanoclusters were the amount of the iron source [7–9], the effect of precipitating agents [9–11], the amount of water content [9,12], the effect of binary solvent ratio [13–15], the reaction time [16,17,7], the different amounts of surfactants [11,12,14,15,17,9], the different types of surfactants [18],

* Corresponding author.
E-mail address: kinnariparekh.rnd@charusat.ac.in (K. Parekh).

https://doi.org/10.1016/j.jmmm.2023.171656
Received 16 October 2023; Received in revised form 10 December 2023; Accepted 20 December 2023
Available online 23 December 2023

and the pH of the surfactant [19]. From these, Hermosa et al. [9] reported the tuning of the nanocluster's size from 117.7 nm to 217.6 nm by changing (i) the iron source, (ii) the amount of precipitating agent, (iii) the addition of different amounts of water, and (iv) the amount of surfactants. Liu et al. [7], Kim et al. [8], and Leshuk et al. [10] studied the Brunauer-Emmett-Teller (BET) surface area and Barrett-Joyner-Halenda (BJH) model for porosity measurement. Kim et al. [8], reported the porous structure of the nanoclusters with the micropores and mesopores, which indicates the type IV isotherm. Leshuk et al. [10] reported that the surface area and porosity results of nanoclusters synthesized by ammonia and urea were comparable with the theoretical results. Chen et al. [13] reported the size of the iron oxide nanospheres from ~ 100 to 700 nm, tuned by changing the ratio of the binary solvents ethylene glycol (EG) and diethylene glycol (DEG), which indicates that as the DEG content increases, the size of the nanoclusters decreases. Zhang et al. [20] reported the synthesis of monodispersed $Mn_xZn_{1-x}Fe_2O_4$ (x = 0.2, 0.4, 0.6, 0.8, 0.9) magnetic nanoclusters using the hydrothermal route, and the results showed that the size of the fabricated nanospheres was 100–200 nm and the saturation magnetization of the samples was related to the degree of Zn^{2+} substitution.

Among all this literature, the MFH study using monodispersed iron oxide nanoclusters [11,12,14,18] is very limited, and there are no reports available for the monodispersed $Mn_{0.5}Zn_{0.5}Fe_2O_4$ composition or its magnetic fluid hyperthermia study. Similarly, the structural, morphological, and magnetic properties don't cover the small angle X-ray scattering (SAXS) and ultra-small angle X-ray scattering (U/SAXS) analyses in correlation with BET measurements of monodispersed magnetic nanoclusters.

The present work reports the maneuvering of $Mn_{0.5}Zn_{0.5}Fe_2O_4$ (A55) composition nanoclusters (nanoflowers) synthesized using the hydrothermal method and their dispersion using tetramethyl ammonium hydroxide (TMAOH) as a surfactant. The size of nanoclusters is tuned by altering the reaction time of the synthesis, which varies from 107 nm to 218 nm. The physical properties of the synthesized samples were studied by XRD, TEM, DLS, and U/SAXS. The magnetic properties of the samples were determined by the VSM, whereas the coating of TMAOH was confirmed via FTIR and TGA. The morphological characterization confirms the porous structure of the nanoclusters, and the porosity was determined by the BET measurement. The synthesized magnetic nanoclusters were further studied for magnetic fluid hyperthermia applications. The optimum value of SAR is explained using all these techniques.

2. Experimental

Iron (III) chloride hexahydrate ($FeCl_3\,6H_2O_{(s)}$, 98 %), manganese (II) chloride tetrahydrate ($MnCl_2\,4H_2O_{(s)}$, 98 %), and tetramethylammonium hydroxide (TMAOH, $N(CH_3)_4^+OH^-$, ≥98 %) were purchased from Sigma Aldrich. Sodium acetate trihydrate ($CH_3COONa\,3H_2O$, 99.5 %) was purchased from Merck; ethylene glycol ($C_2H_6O_2$, 99 %) was from Samir Tech-Chem Pvt. Ltd., India, and zinc (II) chloride ($ZnCl_2$, 98 %) was purchased from LOBA Chemie Pvt. Ltd., India. All these reagents were used without any further purification.

2.1. Synthesis protocol

The hydrothermal route was used to synthesize the manganese-zinc-ferrite magnetic nanoclusters. For the synthesis, $FeCl_3\,6H_2O_{(s)}$, $ZnCl_{2(s)}$, and $MnCl_2\,4H_2O_{(s)}$ salts were taken in the molar ratio of 2:0.5:0.5. The metal ion salts (14.8 mM) and sodium acetate trihydrate (0.106 M) were dissolved in 160 mL of ethylene glycol. The mixture was mechanically stirred for 30 min at room temperature, then transferred into the Teflon-lined stainless steel autoclave container and placed inside the oven (Lab Fine, Sun Instruments Pvt. Ltd., India). The samples were heated at 473 K for different times, viz., 5, 6, 12, 16, or 24 h. Finally, the samples were collected once they reached room temperature. The impurities were removed from the sample by a water wash. After washing, one third of the slurry was taken for coating with TMAOH, and the other two thirds were dried at 333 K in an oven and labeled as uncoated samples. 50 mL of 2.7 M TMAOH solution was added to the 1/3rd slurry, and it was dispersed by sonication for one hour and then left overnight. This process was repeated twice and then followed by magnetic sedimentation to remove the excess TMAOH solution from the sample. The coated particles were redispersed in 30 mL of distilled water using 1 h of sonication to prepare the stable colloidal suspension. The samples were labeled as A55HT5, A55HT6, A55HT12, A55HT16, and A55HT24, respectively, for 5, 6, 12, 16, and 24 h of reaction time during the synthesis. The stock suspension was prepared with a cluster concentration of 1.7 mg/mL.

2.2. Characterization

Powder X-Ray Diffraction (XRD) (Bruker, D2 PHASER, Germany) with Cu K_α radiation (wavelength $\lambda = 0.15418$ nm) was used to determine the crystallite size, crystal structure, phase purity, and lattice parameter of the magnetic nanoparticles. The measurements were made in a 2θ range from 15° to 65° in 0.05° increments. The XRD is equipped with the LYNXEYE detector.

Fourier Transformed Infrared Spectroscopy (FTIR, Nicolet, Thermo Scientific, USA) was used to determine the presence of TMAOH coating on the surface of magnetic nanoparticles (MNPs). The sample was prepared by making a thin pellet of the particles with KBr in the ratio of 1:100. The background of KBr was subtracted from all the data, and the measurements were taken between 400 and 4000 cm^{-1}.

The binding percentage of the surfactant on the particle surface was examined using a thermogravimetric analyzer (TGA, Mettler Toledo, Switzerland). The measurements were performed from 298 to 773 K at a 10 K/min heating rate in a nitrogen gas environment.

TEM samples were prepared by diluting the stock suspension of 1.7 mg/mL to 1000 times in milliQ water. Both, the stock suspension and its dilution were sonicated at least for 30 min before preparing the sample. The collagen-coated copper grid was used to prepare samples for the measurement. A small amount of sample was placed on the grid and then dried in a vacuum for about 24 h. JEOL JEM-2100 with LaB6 filament accelerated at 200 kV was used to measure the microscopic images of the samples. The microscopic images of all the samples were used to determine the cluster size and cluster size distribution using "ImageJ" software. The image was first calibrated with the known distance. Once the calibration was done, an appropriate shape for the nanocluster was selected. The same process was done for all the images to measure the size of the cluster. The size distribution of the samples was calculated using the lognormal distribution function using ~ 150–200 data points. The Fast Fourier Transform (FFT) image and indexing of the FFT pattern was done using "Gatan Microscopy Suite Software (GMS)". The steps were (i) calibrate the images; (ii) generate the FFT pattern; (iii) determine the d-spacing value of the samples using these FFT patterns; and (iv) compare these d-spacing values with those determined from the XRD indexing.

The colloidal properties of samples were measured using a dynamic light scattering (DLS Nano-S90, Malvern) instrument to determine the average hydrodynamic size of the clusters and their polydispersity. The measured sample had a concentration of 0.15 to 0.3 mg/mL, which was achieved by diluting the stock suspension in 1 M ammoniated water. The stock suspension was sonicated for 10 min prior to its dilution. After the dilution, the mixture was sonicated for 10 min. The measurements were carried out at 298 K.

The stability and surface charge of the colloidal particles were measured using a Zeta NanoBrook (90PlusPALs, Brookhaven, USA) Zeta sizer. The measurement was carried out at 298 K. The stock suspension was sonicated for 10 min, then 100 μL of stock suspension was diluted to 1 mL using distilled water. The pH of the suspension was found to be 10.5. The zeta potential of the sample was measured using a poly (methyl methacrylate) (PMMA) cuvette and a resistant electrode probe.

X-ray scattering data were collected on a laboratory-based

instrument, Xenocs-Xeuss 2.0, at the Multiuser SAXS Center EMUSAXS, located at the Institute of Physics, University of São Paulo. This instrument has a Cu anode microfocus X-ray source (Genix3D), FOX3D X-ray mirrors, and two sets of Xenocs scaterless slits. The monochromatic and collimated incident X-ray beam has a wavelength of 0.15419 nm and a square cross section of 0.7 mm in the sample position. The measurements were performed in transmission geometry. The 2D X-ray scattering patterns were measured in a Pilatus 300 K detector at a sample-to-detector distance of about 6.5 m (USAXS) and 1.2 m (SAXS). The 2D images are integrated using the program packages pyFAI [21] and FabIO [22]. Normalization factors are obtained from the direct beam measurements automatically performed during the acquisition. The samples of magnetic fluids were transferred into cylindrical mark-tube capillaries of 1.5 mm diameter and sealed to prevent sample evaporation. For each sample, the measurements were carried out immediately after sealing the capillary to prevent sample sedimentation effects. Each sample was measured twice for 300 s to check for possible changes in the scattering curves. The 2D scattering patterns were frame integrated, resulting in curves of X-ray scattering intensity as a function of the momentum transfer modulus, $q = (4\pi/\lambda)\sin\theta$, where 2θ is the scattering angle. Background and noise subtractions were applied to each curve, with water being used as the background matrix. The USAXS and SAXS 1D profiles were combined in a single scattering curve for further data analysis.

The surface area and porosity of the samples were measured using a BET instrument (Micromeritics, ASAP 2010, USA). The samples were loaded into a sample tube and degassed at 413 K for 6 h with a ramp of 278 K/min in vacuum. Once the degassing was completed, the samples were placed into a liquid nitrogen bath at 78.65 K for the adsorption–desorption isotherm curve, surface area, pore diameter, and pore volume measurements.

The magnetic properties of uncoated and coated clusters were measured with a vibrating sample magnetometer (VSM, LakeShore Model 7404, USA) at room temperature (300 K) in the magnetic field range from −1.2 T to 1.2 T. The magnetization of all the fluid samples was also performed in the field range of 0 to 1.2 T to determine the magnetization of the magnetic fluid. The protocol for the measurement was set in such a way that we could determine the accurate value of the initial susceptibility and saturation magnetization of the sample.

For dry cluster samples, a full hysteresis loop was measured from (i) 0 to 1.2 T field, (ii) 1.2 T to 0 field, (iii) 0 to −1.2 T field, (iv) −1.2 T to 0 field, and (v) 0 to 1.2 T field in a sequential manner with a definite increment in the field value. A typical step followed during the measurement is mentioned here for the first quadrant, and the same is followed for other quadrants too. The initial steps from 0 to 0.0025 T field are increased in the step size of 0.0001 T field; from 0.0025 to 0.01 T, the step size of 0.0025 T was kept; from 0.01 to 0.3 T, the increment was 0.025 T, from 0.3 to 1.0 T, the step size was set to 0.05 T; and from 1.0 to 1.2 T fields, the step size was set to 0.01 T.

The protocol was changed for the magnetic fluid samples as compared to the dry cluster samples for two reasons: (i) clusters will have the freedom to physically rotate in the fluid; (ii) within nanoclusters, the particles will experience torque from an external magnetic field. In the case of magnetic fluid samples, the measurement is done only in the virgin curve, i.e., the first quadrant. The steps in the initial magnetic field were adjusted to increase by 0.0001 T field up to the field of 0.0025 T, and then a larger step size of 0.00025 T was set from 0.005 to 0.01 T field. From 0.01 to 0.1 T, the step size was 0.001 T, while the increment in the field was set to 0.005 T from 0.1 to 1.2 T.

The magnetic fluid hyperthermia (MFH) experiment was performed using an induction heating system, Easy Heat LA-8310 (Ambrell, USA). The set-up of the MFH includes the induction heating coils, biosafety cabinet, power supply for the biosafety cabinet, optical fiber sensor, and water chiller to maintain the temperature of the coil. The instrument can operate at 10 kW with a fixed frequency of 333 kHz and a variable magnetic field from 0 to 15 kA/m. The coil used for the MFH study is a 2 x 2 turn Helmholtz coil with an inner diameter of 0.06 m. The induction heating experiment is used to study the heating response of the samples under the exposure of an alternating magnetic field (AMF) of high frequency. The sample was first sonicated for 30 min, and then 1 mL of sample was taken from the parent sample into the sample holder and placed in the center of the induction heating coil. The sample holder (vial) is insulated with the rubberized cork sheet so as to prevent it from radiating heat. The required amount of current is passed through the coil so as to generate a 10 kA/m magnetic field, which is connected to the high-frequency AC field generator that eventually heats the sample over a time span. The initial temperature is fixed at 303 K, and then the change in temperature is measured using the optical fiber sensor.

3. Results and discussion

In the present work, we discussed the effect of reaction time (5, 6, 12, 16, and 24 h) during the hydrothermal synthesis of $Mn_{0.5}Zn_{0.5}Fe_2O_4$ nanoclusters and their suspension in distilled water on the physical and magnetic properties of the samples. After the synthesis of nanoclusters, the aliquot of the sample was dried (2/3rd part) and used for the structural characterization. Similarly, after TMAOH coating, the aliquot of the coated sample was dried. Both, uncoated and coated dry samples were characterized using XRD, TGA, FTIR, BET, and VSM. Whereas, the suspension of TMAOH nanoclusters in distilled water was characterized for TEM, DLS, zeta potential, U/SAXS, VSM, and induction heating instrument. The results of the same are discussed below.

3.1. XRD study

Fig. 1a displays the XRD pattern for all the samples. The diffraction pattern confirms the single-phase cubic spinel structure for all the samples. The peaks at 18.19°, 30.03°, 35.45°, 43.1°, 53.42°, 56.92°, and 62.43° correspond to the (111), (220), (311), (400), (422), (511), and (440) planes, confirming the face-centered cubic (FCC) spinel structure of the samples. No extra peaks were observed in any of the samples, which indicates the purity of the sample. The crystallite size and the lattice parameter were obtained by fitting the data using MAUD refinement software [23]. The XRD pattern for all samples fits the Fd-3 m space group with an inverse spinel structure. The MAUD-refined XRD pattern of the A55HT24 sample is shown in Fig. 1b. The crystallite size calculated from refinement varied from 13.8 to 19.3 (±0.3) nm, respectively, for the obtained samples, where the heating time increased from 5 h to 24 h. The size of each sample is mentioned in Table 1. From the results, it is observed that as the reaction time increases, the crystallite size of the particles increases. It was observed that the crystalline phase doesn't form when the reaction time is less than 5 h. Also, keeping the reaction for 30 h doesn't improve the crystallinity or size of clusters. The lattice parameter of all the samples is between 0.8403 and 0.8428 (±0.0002) nm. The observed lattice constant value is near to that reported for $Mn_{0.5}Zn_{0.5}Fe_2O_4$ (0.8421 nm) [24].

3.2. FTIR and TGA study

The coating of TMAOH was confirmed using FTIR and TGA. Fig. 2 represents the FTIR results of synthesized MNPs after TMAOH coating along with pure surfactant, i.e., TMAOH. The strong and broad peak around 3400 cm^{-1} is assigned to the hydroxyl group in the samples. The peak at 1600 cm^{-1} represents H-O-H bending. The other single band that appears at 950 cm^{-1} is due to the asymmetrical stretching of the C-N bond [25]. The band between 2900 and 3000 cm^{-1} is assigned to C-H symmetrical and asymmetrical stretching, whereas peaks between 1400 and 1500 cm^{-1} are due to C-H symmetrical and asymmetrical bending. The intense peaks in the fingerprint region of 400–600 cm^{-1} are the characteristics of metal oxides (Me-O) at the tetrahedral (A) sites and octahedral (B) sites of spinel ferrite [26]. The other peaks in the region of 600–4000 cm^{-1} in coated MNPs indicate the surfactant peak.

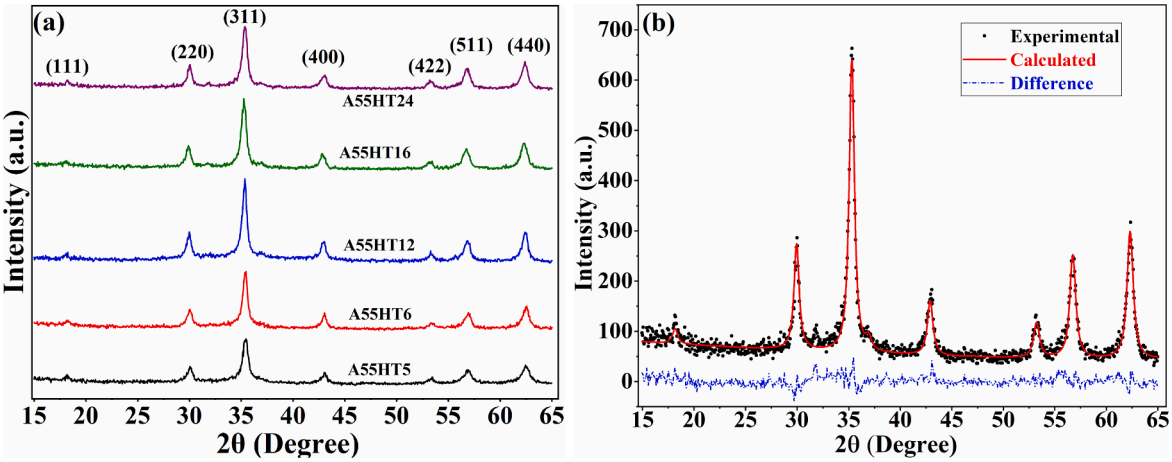

Fig. 1. (a) X-ray diffraction pattern for $Mn_{0.5}Zn_{0.5}Fe_2O_4$ samples synthesized using the hydrothermal route at different reaction times. (b) Refinement of XRD pattern using MAUD software for A55HT24 sample.

Table 1
Crystallite size, cluster size and hydrodynamic size of samples.

Sr. No.	Sample Name	XRD results	TEM results		DLS results	
		D_{XRD} (nm)	D_{TEM} (nm)	σ	D_H (nm)	σ
1	A55HT5	13.8 ± 0.3	158.1 ± 1.7	0.09	160.0 ± 0.5	0.37
2	A55HT6	18.1 ± 0.4	218.3 ± 3.1	0.11	201.3 ± 0.9	0.37
3	A55HT12	18.5 ± 0.3	208.5 ± 2.4	0.12	194.8 ± 0.9	0.40
4	A55HT16	19.2 ± 0.3	106.8 ± 1.3	0.10	112.7 ± 0.5	0.36
5	A55HT24	19.3 ± 0.3	114.8 ± 1.9	0.09	113.5 ± 0.3	0.31

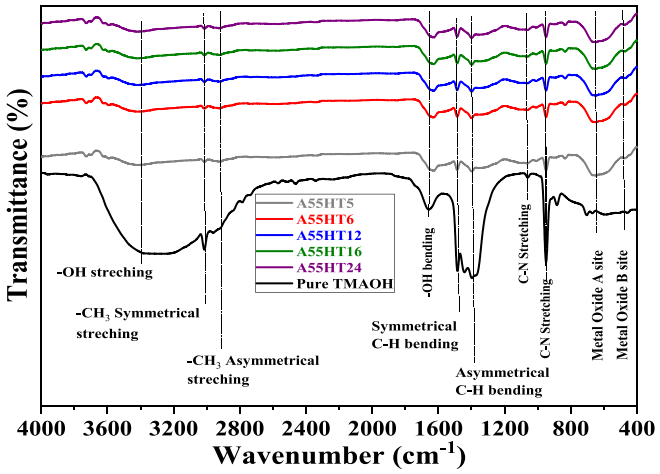

Fig. 2. FTIR spectra of TMAOH (black line) with coated MNPs.

The thermogravimetric analysis of TMAOH-coated samples measured between 298 and 773 K is shown in Fig. 3. The weight loss of TMAOH-coated particles was found to be different for all samples synthesized at different reaction times. The total weight loss of all the samples is around 31 %, 12 %, 5.4 %, 10 %, and 9 %, respectively, for 5 to 24 h of reaction time. It is to be noted here that the samples A55HT5 and A55HT12 are two samples that have two extreme weight losses, respectively, a maximum and a minimum, as compared to other samples. The observed difference in weight loss may be correlated with the

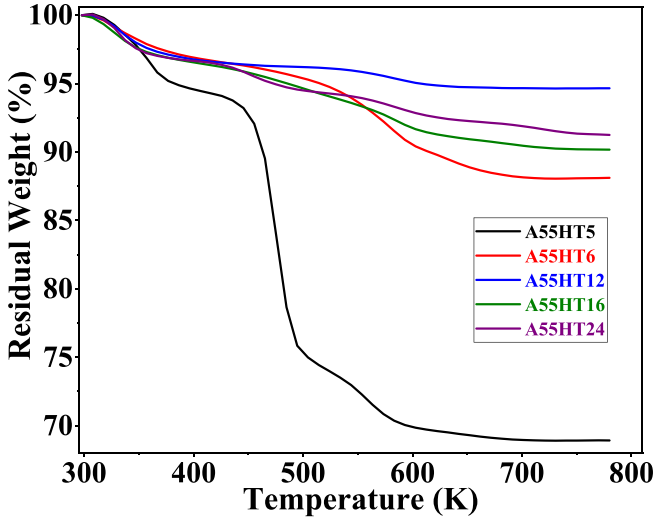

Fig. 3. TGA weight loss plot of TMAOH coated samples.

availability of the surface area of the clusters. For the A55HT5 sample, we believe that more surfactant must have bound to the nanoclusters, whereas for the A55HT12 sample, it could be a lesser amount. However, it is difficult at this point to exactly pinpoint the reason. It is seen that the transition occurred in multiple steps throughout the temperature range of 298 to 773 K. The first weight loss up to 373 K in all the samples is attributed to the water molecules and moisture adsorbed on the particle surface. Whereas, the weight loss between 373 and 473 K can be due to the bound OH^- to the surface of MNPs. The third weight loss observed around 573 K is assigned to the oxidative removal of TMA^+ cations bonded to the nanoparticle surface [27].

3.3. TEM study

The morphology and the size of the nanoclusters were determined using transmission electron microscopy images. The TEM images of the samples A55HT5, A55HT6, A55HT12, A55HT16, and A55HT24 are shown in Fig. 4 (a-e), respectively. The image reveals that all samples are spherical and have very uniform-sized nanoclusters. The TEM images at high magnification of the samples are shown in Fig. 4 (f-j). They revealed that clusters were composed of a large number of small-sized nanoparticles. Fig. 4 (k-o) shows the cluster size (*D*) distribution fitted (red line) with a lognormal distribution function, $f(D)\,dD$ (Eq. (1)).

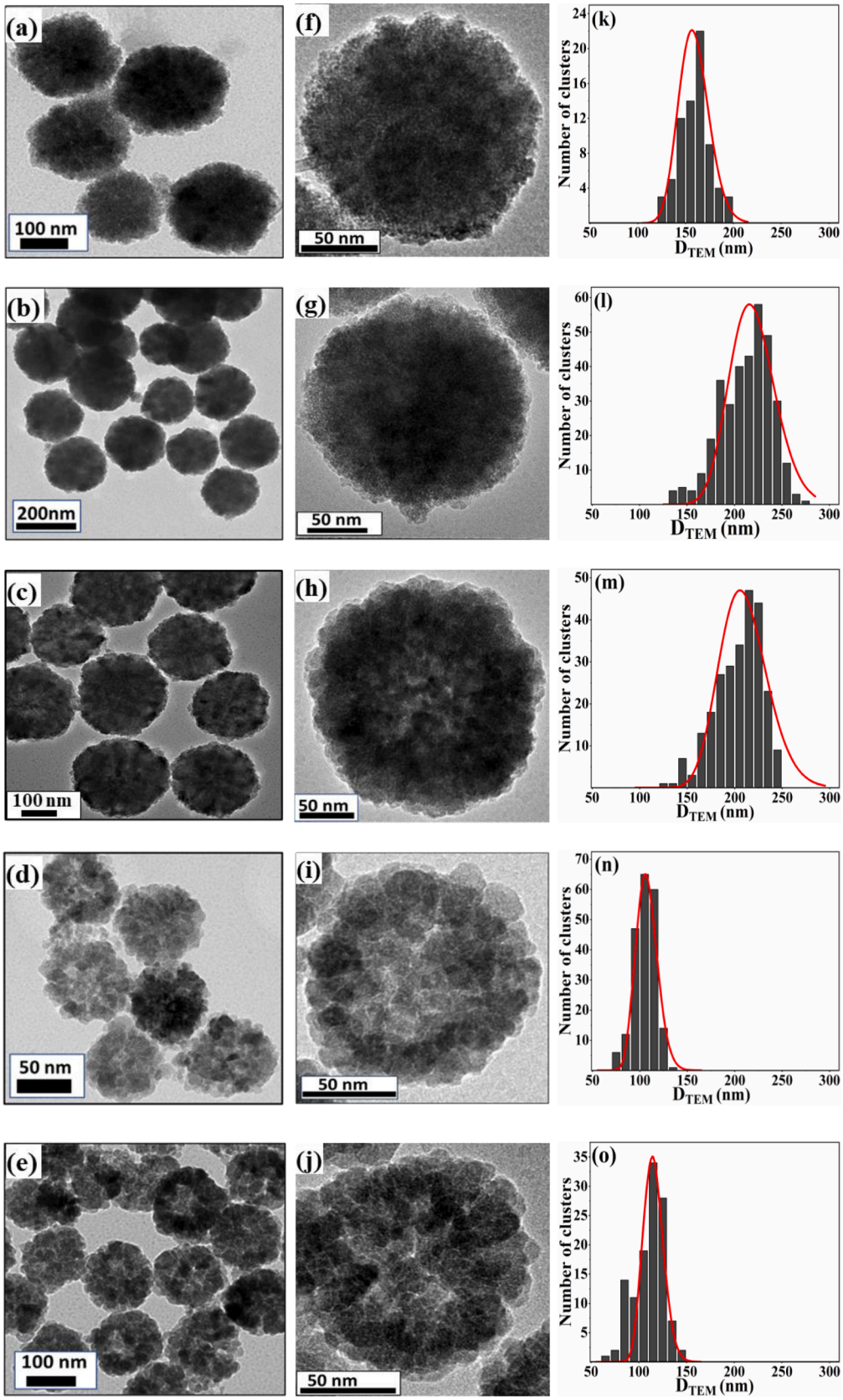

Fig. 4. TEM image of the particles prepared at different reaction time (a) to (e); higher magnification TEM image of nanoclusters (f) to (j); nanoclusters size distribution (k) to (o), corresponds to the A55HT5, A55HT6, A66HT12, A55HT16 and A55HT24 samples.

$$f(D) \bullet dD = \frac{1}{\sqrt{2\pi}\sigma D}.exp\left(\frac{-ln\left(\frac{D}{D_0}\right)^2}{2\sigma^2}\right) \quad (1)$$

Where, D_0 is a mean cluster size and σ is a standard deviation in cluster size. The mean cluster size and size distribution obtained for each sample are shown in Table 1. It is seen that as the reaction time increases from 5 to 6 h, the mean size of clusters increases from 158.1 nm to 218.3 nm, and then it decreases to 106.8 nm. and reaching equilibrium with the further increase in time up to 24 h.

It is seen from Fig. 4 (k) to 4 (o) that the nanoclusters size is shifted from higher (150–300 nm) to lower (50–150 nm) values, as the time of reaction increases from 6 h to 24 h. This is because initially at 5 h, the particles within a cluster just nucleated and start aggregating to form a cluster to minimize the surface energy. Then, slowly the crystallinity of these nucleated particles increases as the maturity of the reaction progressively increases with the time. This will re-distribute the size of the clusters between 100 and 300 nm. Once the particles within a cluster are matured enough and reaching to a state of equilibrium, the growth stops. This is a balancing of surface free energy and dipolar interaction energy between the particles within a cluster leading to an optimal size of the cluster and its porosity after some time. Further increasing the reaction time doesn't change much the size of a cluster or its distribution. In the present case the optimum reaction time is 16 h which leads to a highly porous nanocluster comprises of well crystallized nanoparticles.

A large number of small nuclei are seen in the TEM images of the A55HT5 sample as compared to other samples. This may be a reason to observe higher weight loss in TGA for this sample. In addition, the A55HT12 sample seems to have very porous clusters consisting of few nanoparticles within a cluster, rendering a low surface area to bind the TMAOH, consequently a lesser weight loss in TGA.

Fig. 5 (a-e) displays the HRTEM image with a 5 nm scale bar reflecting the crystalline nature of the clusters. For samples A55HT5, A55HT6, A55HT16, and A55HT24, atomic arrangement of the (311) plane with an inter-planar distance of around 0.25 nm is seen. Whereas, for the A55HT12 sample, the d-spacing value is 0.30 nm corresponds to the (220) plane. The Fast Fourier Transformation (FFT) generated from the HRTEM is shown in Fig. 5 (f-j). The figure produced displays the equidistance dot pattern from the zone axis at a particular distance for various planes. The d-spacing value corresponding to each plane is compared with that of the XRD d-spacing results, and then the FFT image is indexed as shown in the FFT pattern. The resultant d-spacing values obtained from FFT images for all the samples using GMS software are mentioned in Table 2.

3.4. DLS and zeta potential study

The cluster size and its distribution are measured using the intensity distribution observed from DLS measurements. Fig. 6 (a) represents the intensity distribution of the clusters for all samples. The hydrodynamic size of the cluster distribution is then fitted using the lognormal distribution function using Eq. (1). Fig. 6 (b) represents the typical result for A55HT24 sample fitted with the lognormal distribution function (red line). The obtained median diameter and the standard deviation of all the samples are mentioned in the Table 1. It is seen that the hydrodynamic diameter of clusters for all the samples is very close to the diameter of clusters obtained from the TEM images. This may be due to the good compatibility of TMAOH with the distilled water, which creates a very thin layer of water around the clusters, unlike other long-chain surfactants as described by Bender P. et al. [28].

The zeta potential of the samples was measured five times and the average of these measurements is considered. The value of zeta potential of fluids along with the standard deviation at 10.5 pH is found to be −45.11 (±3.7) mV, −44.73 (±1.6) mV, −41.19 (±3.7) mV, −44.21 (±6.6) mV and −46.62 (±2.8) mV, respectively, from the A55HT5 to A55HT24 samples. The zeta potential values of all the samples greater than ± 30 mV indicate the good dispersion stability of the fluid.

3.5. U/SAXS study

The U/SAXS curves for the samples are shown in Fig. 7. The U/SAXS data presents oscillations, which indicate the formation of well-defined particles with low polydispersity [29].

The TEM image for a typical sample of nanoflowers is shown in Fig. 4. One can clearly see that the nanoflowers have a spherical shape and are composed of internal subunits with an overall spherical shape. A model for the U(SAXS) data for the nanoflowers, based on the TEM image, is composed of an overall large spherical particle with internal components. By the analysis of the several datasets, the best fits were obtained under the assumption that the system contains small polydisperse spheres and polymer-like contributions. Therefore, the model used for the scattering intensity is given by:

$$I(q) = Sc_1 I_{CS}(q) S_{HS}(q) + Sc_2 I_{sph}(q) + Sc_3 I_{pol}(q) \quad (2)$$

In this model, Sc_i are the scale factors for the several parts. $I_{CS}(q)$ is the intensity of a large core–shell sphere, with radius R_{CS}, polydispersity, σ_{CS}, shell thickness T and relative contrast of the shell $\Delta\rho_R = \Delta\rho_{shell}/$

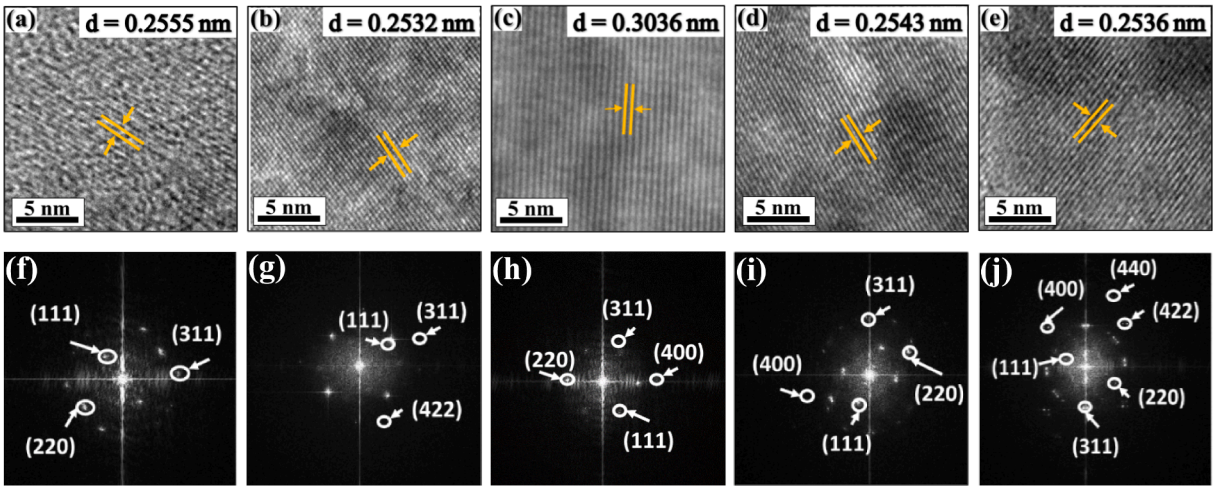

Fig. 5. (a-e) High resolution TEM images of $Mn_{0.5}Zn_{0.5}Fe_2O_4$ samples synthesized at different reaction temperatures; (f-j) Fast Fourier Transform (FFT) pattern of A55HT5, A55HT6, A55HT12, A55HT16 and A55HT24 samples, respectively.

Table 2
d-spacing values obtained from XRD and FFT pattern for all the samples.

(*hkl*)	A55HT5 d-spacing (nm)		A55HT6 d-spacing (nm)		A55HT12 d-spacing (nm)		A55HT16 d-spacing (nm)		A55HT24 d-spacing (nm)	
	XRD	TEM	XRD	TEM	XRD	TEM	XRD	TEM	XRD	TEM
(111)	0.4871	0.4904	0.4844	0.4876	0.4857	0.4671	0.4884	0.4847	0.4871	0.4812
(220)	0.2972	0.2979	0.2972	–	0.2976	0.3011	0.2986	0.2926	0.2972	0.2984
(311)	0.2529	0.2533	0.2529	0.2530	0.2536	0.2526	0.2543	0.2545	0.2536	0.2536
(400)	0.2096	–	0.2099	–	0.2101	–	0.2108	0.1922	0.2096	0.2040
(422)	0.1713	–	0.1716	0.1718	0.1717	–	0.1722	–	0.1719	0.1719
(511)	0.1615	–	0.1615	–	0.1617	–	0.1621	–	0.1618	0.1643
(440)	0.1485	–	0.1483	–	0.1486	–	0.1487	0.1466	0.1486	0.1399

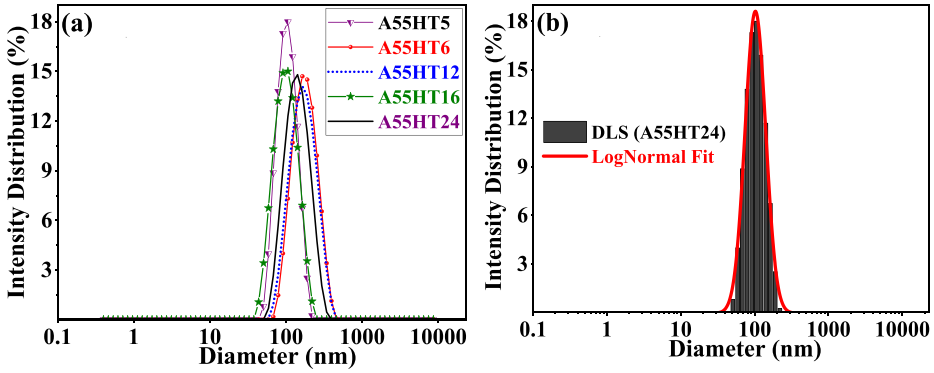

Fig. 6. DLS results of A55HT5 to A55HT24 samples produced at different reaction time displaying intensity distribution as a function of hydrodynamic cluster size. (b) intensity distribution of A55HT24 sample fitted with the lognormal distribution function (red line).

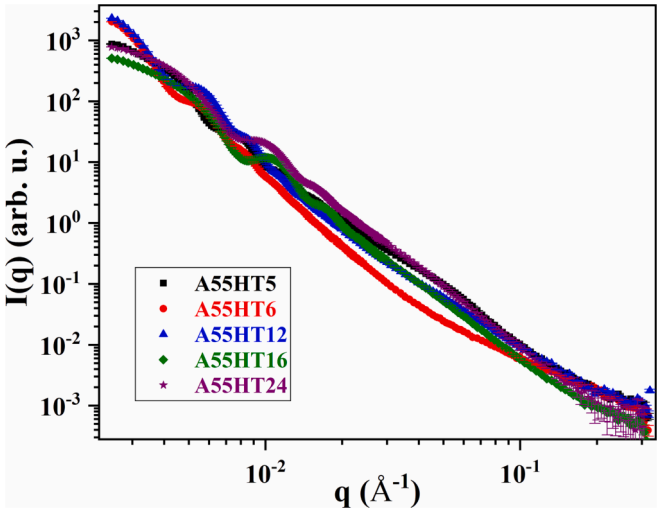

Fig. 7. Treated data for the U/SAXS intensities from the nanoflowers.

$\Delta\rho_{core}$ [30]. The contribution from the small spheres that compose the nanoflowers is given by $I_{sph}(q)$ which is the intensity of polydisperse solid spheres with radius R_S and polydispersity σ_S. The polymer contribution $I_{pol}(q)$ is given by the Debye formula for a Gaussian chain [31] with an overall radius of gyration, R_{Gpol}. In this model the contributions for the large nanoflowers, small spherical inner spheres, and polymers are simply added. Since the size of the nanoflowers is much larger than the inner small spheres, this approximation is good enough for the model fitting. Other models, combining the nanoflowers as aggregate structure factors for the inner small spheres were tried without good improvements in the fit. Therefore, this simpler approach was used. The (U)SAXS data show that the nanoflowers present repulsive interactions, which promote a decrease in intensity at low angles. This is taken into account by the hard sphere structure factor $S_{HS}(q)$, on which one has the volume fraction of the particles η_{HS} and the effective hard sphere radius R_{HS} [30]. A tentative sketch of the model is shown in Fig. 8a.

The model fits are shown in Fig. 8b. Due to the large size of the nanoflowers, smearing effects due to the beam size were taken into account [32], which explains the two curves for each dataset: one passing by all the points and the other slightly off. The actual fitting curve, with smearing effects included, is the one passing by all points, and the original theoretical curves is taken assuming a point-like beam. As can be seen, the fits can describe the main features of the obtained SAXS data.

The obtained model parameters are represented in Table 3. For comparison, in the last two rows of the tables, the overall size obtained from the U/SAXS analysis and the values obtained by the TEM analysis are mentioned. All in all, the values are in good agreement, but the averaging from the U/SAXS data is obtained for a much larger number of particles.

From the data analysis, it was possible to obtain several structural features from the investigated system. Besides the overall size, which is in very good agreement with TEM results, polydispersity levels and details on the internal structure were obtained.

3.6. Particle size distribution within a single cluster

The magnified transmission electron microscopy image at a 20 nm scale bar for a single cluster is displayed in the Fig. 9 (a, b) for the A55HT16 and A55HT24 samples, respectively. It reveals that the cluster is an accumulation of numbers of small nanoparticles. The size of nanoparticles within a cluster is measured using the ImageJ software, and the resultant data are fitted by lognormal distribution function using Eq. (1). The particle size distribution with a lognormal fit (red line) is shown in Fig. 9 (c, d). The resultant size of particles determined for A55HT16 is 19.34 ± 0.16 nm with a standard deviation of 0.06, and for A55HT24, the size was 19.49 ± 0.15 nm with a standard deviation of

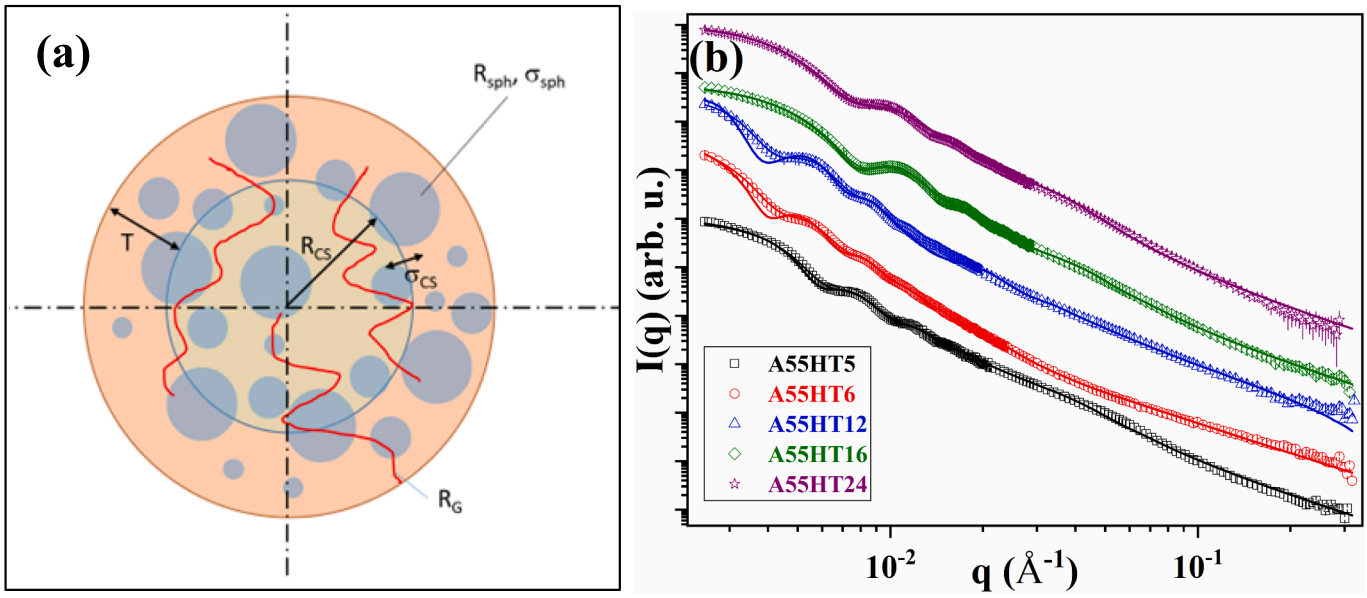

Fig. 8. (a) Sketch of the proposed model, (b) model fits for the investigated samples.

Table 3
Structural parameters obtained from U/SAXS analysis.

Parameters	Sample A55HT5	A55HT6	A55HT12	A55HT16	A55HT24
R_{CS} (nm)	50.0 ± 0.8	68.3 ± 0.6	61.4 ± 0.8	27.9 ± 0.3	29.2 ± 0.4
T (nm)	20.0 ± 0.7	39.5 ± 0.3	42.9 ± 0.5	20.1 ± 0.3	21.6 ± 0.3
σ_{CS} (nm)	7.3 ± 0.2	8.4 ± 0.1	8.3 ± 0.4	4.8 ± 0.7	5.8 ± 0.1
$\Delta\rho_R$	0.81 ± 0.01	0.94 ± 0.01	0.54 ± 0.02	0.57 ± 0.06	0.40 ± 0.02
η_{HS}	0.18 ± 0.01	0.15 ± 0.01	0.26 ± 0.02	0.040 ± 0.02	0.064 ± 0.01
R_{HS} (nm)	52.5 ± 0.1	78.0 ± 0.7	104.0 ± 4.0	33.3 ± 1.1	50.0 ± 2.0
R_{sph} (nm)	~3.5	~3.5	~3.5	~3.5	~3.5
σ_{sph} (nm)	~1.7	~1.7	~1.7	~1.7	~1.7
R_G (nm)	~12.0	~12.0	~15.0	~15.0	~15.0
$Size_{(U)SAXS}$ (nm)	140.0 ± 2.0	216.0 ± 1.0	209.0 ± 2.0	96.0 ± 1.0	102.0 ± 1.0
$Size_{TEM}$ (nm)	158.1 ± 1.7	218.3 ± 3.1	208.5 ± 2.4	106.8 ± 1.3	114.8 ± 1.9
$Size_{DLS}$ (nm)	160.0 ± 0.5	201.3 ± 0.9	194.8 ± 0.9	112.7 ± 0.5	113.5 ± 0.3

0.06. The resultant size of particles is nearly the same as that obtained from the crystallite size of samples using XRD.

3.7. BET measurement

The isotherms of N_2-based adsorption–desorption plots for all samples are depicted in Fig. 10. The resultant curves exhibit a H4 type of hysteresis loop, which indicates the mesoporous structure of the nanoflowers. The BET model was used to measure the surface area and pore volume of the samples. The pore diameter of all the samples was characterized by the BJH (Barrett-Joyner-Halenda) model. The outcomes of mean pore diameter, surface area and pore volume of all the samples are mentioned in Table 4. The results mentioned in Fig. 10 as well as Table 4 indicate that all the samples possess a high surface area and pore volume, confirming the porous structure of the samples. The maximum pore volume of 0.398 cm^3/g is observed in the A55HT16 sample. Whereas sample A55HT12 has a smaller surface area among all samples. This result can be correlated with the observed weight loss from TGA, which is the minimum for this sample. The porous structure of the nanoflowers will have advantage of encapsulating the drug inside them, and then, with external stimuli, it can be released as and when needed.

3.8. VSM study

Fig. 11 (a) represents the room temperature response of specific magnetization (σ_s) as a function of magnetic field (H) for TMAOH-coated cluster samples characterized using VSM. It is seen that the clusters are showing superparamagnetic behavior at room temperature; the zoom image of the samples near to origin shows zero coercivity and remanence in all the samples (refer the inset Fig. 11a). Similarly, the magnetic response of uncoated clusters is also measured. Fig. 11 (b) displays a typical comparison of coated and uncoated clusters for the A55HT24 sample. The data were taken in small steps (0.0001 T) near origin and the saturation (steps of 0.01 T) so that the accurate value of initial susceptibility and saturation magnetization could be determined. The initial susceptibility of the samples was determined by taking the slope of the initial curve of the hysteresis loop in the low-field region (0–0.0025 T). The saturation magnetization of the particles is determined from the intercept of the M versus 1/H curve. The resultant values of initial susceptibility (χ_{ini}) and saturation magnetization (M_s) of uncoated and coated clusters are shown in Fig. 11 (c) and 11 (d), respectively. The saturation value of specific magnetization of the coated clusters is higher than that of the uncoated clusters as observed from Fig. 11 (d) except for the A55HT5 sample, which has a lower saturation magnetization for coated clusters than the uncoated clusters. The reduction in Ms for A55HT5 sample may be due to the presence of an excess amount of surfactants as seen from the TGA results. The initial susceptibility (mass) is also increased with coating for all the samples, which may be due to the reduction in the particle–particle interaction.

Fig. 12 displays the magnetic response of TMAOH-coated A55HT5, A55HT6, A55HT12, A55HT16, and A55HT24 magnetic fluid samples. The asymptotic behavior of the fluid sample is fitted using the core–shell model [33] where a magnetic particle is assumed to have a magnetically dead layer on the surface of the particle whose magnetic response is not as similar as its core. This dead layer, along with the surfactant thickness, contributes to the paramagnetic susceptibility. Hence, an existing Langevin's theory for superpamagnetic particles is modified using this. The same is described as below.

For the core–shell model, we assume a particles volume distribution

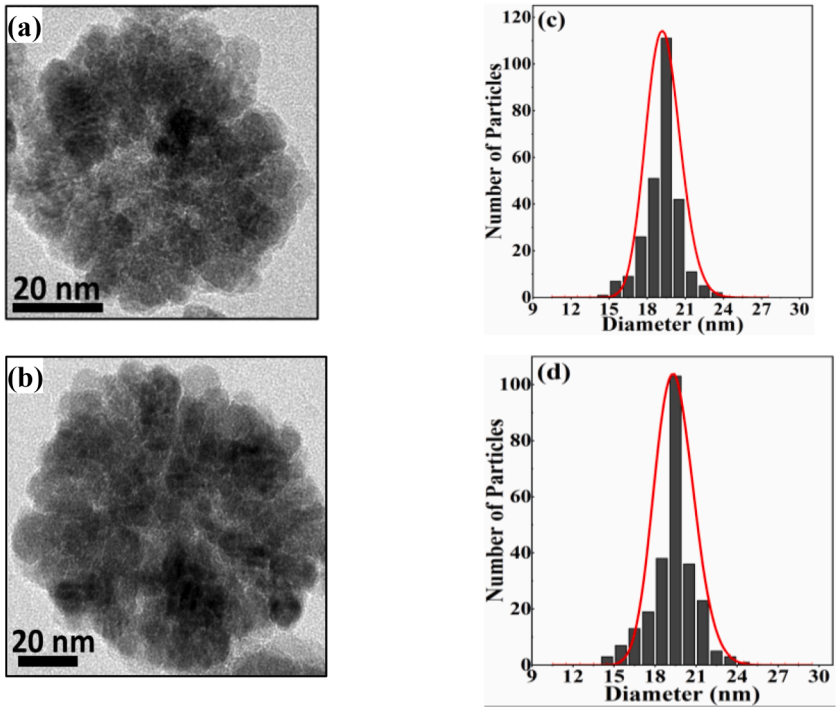

Fig. 9. Higher magnification TEM images of magnetic nanoclusters and particles size distribution within the clusters (a, c) 16 h, (b, d) 24 h.

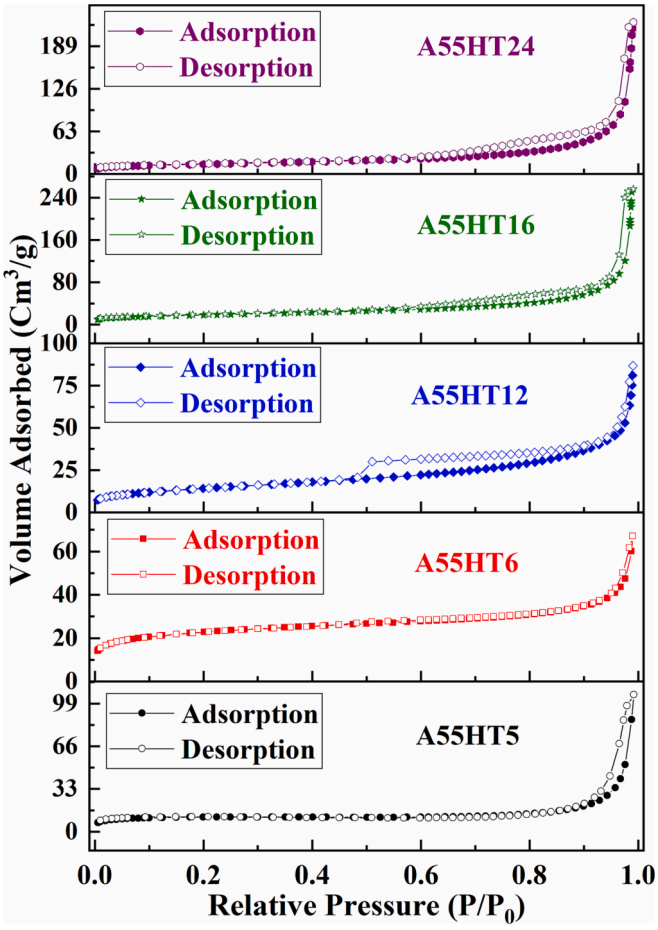

Fig. 10. The N_2 Adsorption-Desorption isotherms curve of all the samples.

Table 4
Mean pore diameter, surface area and pore volume of nanoclusters synthesized at different reaction time.

Sr. No.	Sample Code	Pore diameter (nm)	Surface area (m^2/g)	Pore volume (10^3 m^3/kg)
1	A55HT5	19.78	43.8 ± 0.1	0.165
2	A55HT6	5.12	83.3 ± 0.3	0.104
3	A55HT12	8.87	43.4 ± 0.4	0.135
4	A55HT16	23.43	61.6 ± 0.4	0.398
5	A55HT24	25.4	50.0 ± 0.3	0.349

with the log-normal probability density function as expressed in Eq. (4)

$$f(V) \bullet dV = \frac{1}{\sqrt{2\pi}\sigma V}.exp\left(\frac{-ln\left(\frac{V}{V_0}\right)^2}{2\sigma^2}\right) \quad (4)$$

Where V_0 and σ are the mean volume and standard deviation of volume, respectively. In the magnetization curve of M versus H, the core–shell model is expressed by Eq. (5)

$$M(H)f(V) = \int_0^\infty f(V) \bullet \left[M_s L(\alpha) + \chi_{pm} H\right] dV \quad (5)$$

Where L(α) is the Langevin function, L(α) = coth (α) – 1/α. Here, $\alpha = \frac{M_s VH}{k_B T}$, the magnetic particle size, D_{mag}, is calculated using, $D_{mag} = \left(\frac{6}{\pi V_0}\right)^{\frac{1}{3}}$ and size distribution, $\sigma_D = \frac{\sigma}{3}$. The paramagnetic susceptibility (χ_{pm}) is due to the paramagnetic shell's finite thickness of 0.134 nm. The magnetization curve was fitted using a core–shell model as expressed in Eq. (5) and the magnetic parameters such as the magnetic size of the particle (D_{mag}), magnetic size distribution (σ_D), saturation magnetization (Ms), and paramagnetic susceptibility (χ_{pm}) were obtained by keeping the domain magnetization of the particles ($Mn_{0.5}Zn_{0.5}Fe_2O_4$ composition) fixed at 740 kA/m [34], k_B = 1.38x10^{-23} J/K, the measurement temperature T = 298 K as constant, and the resultant values of

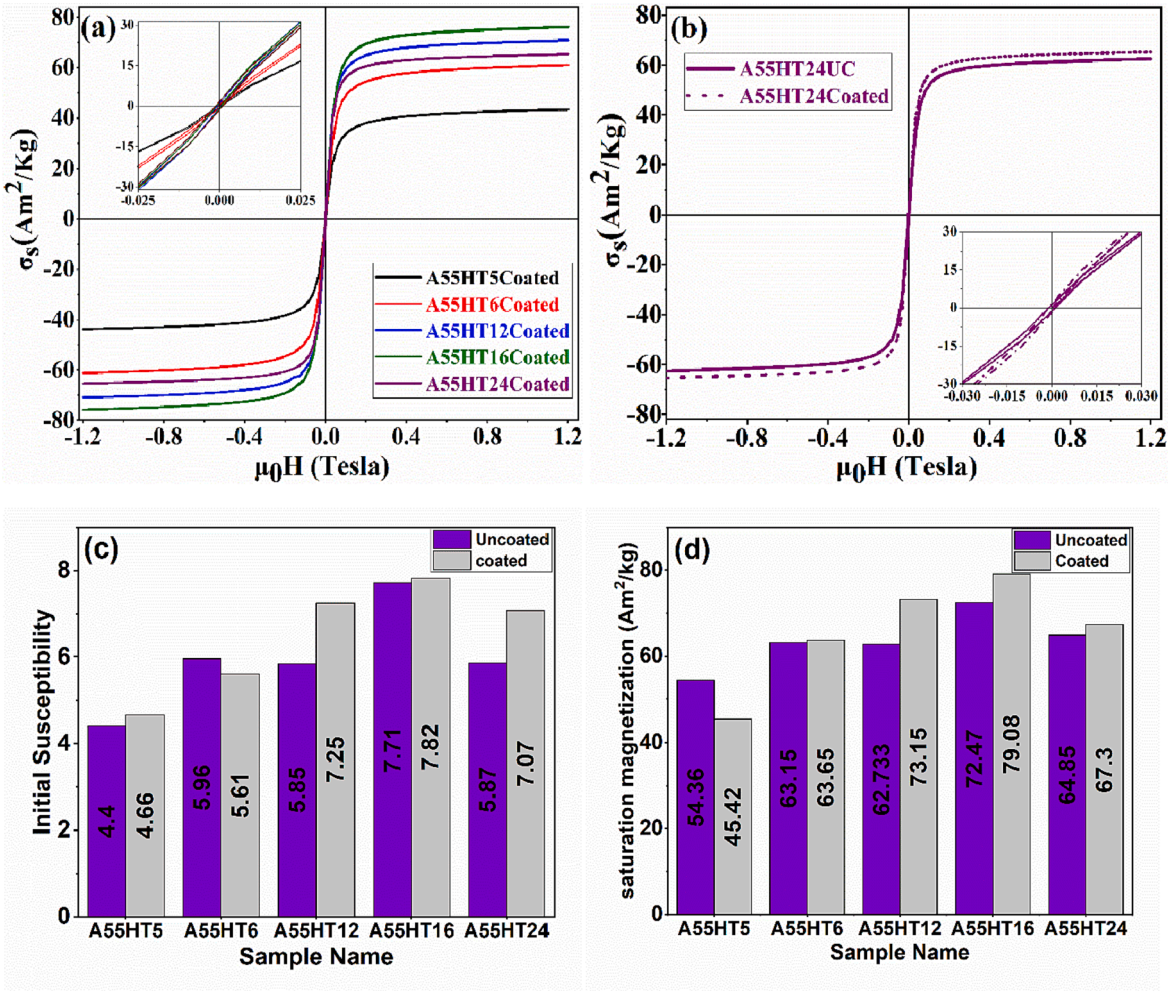

Fig. 11. Magnetic response of (a) TMAOH coated samples (b) uncoated and coated A55HT24 cluster sample. (c) initial susceptibility of uncoated and coated cluster samples (d) saturation magnetization of uncoated and coated cluster samples.

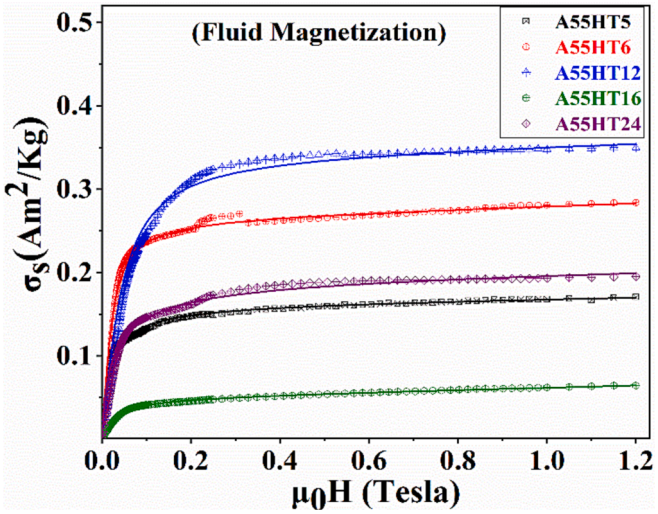

Fig. 12. Magnetic measurement curves of fluid samples (symbols) fitted with the core–shell model (solid line).

the samples are mentioned in Table 5. The magnetic diameter obtained by such fitting matches the crystallite size obtained from XRD except for sample A55HT12. However, the polydispersity of these particles is

Table 5
Results of magnetic parameters determined from core-shell model fit.

Sample	D_{mag} (nm)	σ_D	Ms (Gauss)	χ_{pm}
A55HT5	13.04	0.40	2.28	1.0×10^{-4}
A55HT6	10.36	0.10	3.58	3×10^{-4}
A55HT12	7.48	0.10	4.99	4.5×10^{-5}
A55HT16	14.59	0.49	0.72	2.1×10^{-4}
A55HT24	18.34	0.66	3.09	1.0×10^{-4}

observed to be high due to a collective effect of (i) the number density of particles, (ii) the porosity of nanocluster, (iii) dipolar interaction between particles in a nanocluster. A detail and rigorous study is warranted in future in this direction. We believe that the magnetic diameter may be the effective diameter of the core of a cluster of a few hundred nanometers. Upon application of the magnetic field, the constituent particles rotate themselves in the field direction, and resulting in the overall increase in magnetization upon increasing magnetic field strength. The contribution of paramagnetic susceptibility needs to be included to achieve the best fit.

An interesting behavior in the magnetization curve (Fig. 12) is observed: a "shoulder" appears at the intermediate field in the M−H curve, which is more pronounced in samples A55HT6, A55HT12, and A55HT16. In samples A55HT5 and A55HT24, this behavior is barely seen. A non-monotonic increase in the magnetization is present in the curves as the field increases. This type of behavior is neither expected

nor observed in single-particle ferrofluids. A possible origin of this behavior could be the Brownian rotation of the individual particles inside the particle's cluster, imposed by the external magnetic field. If the magnetic torque acting on the particle's magnetic moment exceeds the particle–particle interaction forces inside the cluster, the particles inside the cluster may rotate to better align their magnetic moments to the external field. This process leads to an increase in the magnetization value, and this type of behavior is not expected in case the particles are hindered from rotating. The interparticle forces may depend on the synthesis conditions and coating of the clusters and could explain the more pronounced behavior in some of the samples we analyzed. However, a more systematic study is necessary to explain this phenomenon.

3.9. MFH study

Induction heating characteristics of samples are measured at constant frequency of 333 kHz and 10 kA/m magnetic field which is less than the safety limit. The aim of performing the hyperthermia study is to see that which sample satisfies the criteria of achieving the magnetic fluid hyperthermia window temperature of 315–318 K within the safety limit [35] of $H{\cdot}f = 5{\cdot}10^9$ $Am^{-1}s^{-1}$ with the minimum concentration of particles. The concentration of magnetic fluid was fixed at 1.7 mg/mL to measure the heating efficiency of magnetic fluid. According to the Rosensweig's model [2], power (P) dissipated per unit mass is given by Eq. (6),

$$P = \mu_0 \omega H_0^2 \chi_0 f H^2 \frac{\omega\tau}{1+\omega^2\tau^2} \tag{6}$$

Here, ω and χ_0 indicates the frequency and initial susceptibility. The induced heat is quantified by the specific absorption rate (SAR) which is the heat generated per unit mass (W/g) of a sample. In terms of the experimental estimation, it depends on the rise in temperature of magnetic fluid as a function of time under the constant magnetic field and frequency. The initial rate of temperature rise and the saturation temperature can be obtained using the Box-Lucas fit [36] to the experimental data and the product of this yield denotes the value of dT/dt (slope of Temperature versus time plot), which is utilized to compute the SAR. The hyperthermic response data is fitted using the Box-Lucas model Eq. (7) given by,

$$T(t) = A\left(1 - e^{-Bt}\right) \tag{7}$$

Where, T (t) is a temperature with respect to time t, A is the saturation temperature and B is the heating rate. The temperature rise with respect to time for all samples fitted using Box-Lucas Eq. (7) is displayed in Fig. 13(a) (solid line). It is seen from the figure that the temperature rises asymptotically and then reaching to a saturation due to a fact that induction heating is an adiabatic heating process. This is a typical behavior observed when magnetic particles acquire heat as a result of moment fluctuations brought on by either Neel or Brownian rotation in the liquid dispersion. In contrast to the regular behavior (smooth growing behavior), the atypical behavior (discreteness) is observed at the intermediate time in nearly all of the samples. This might be due to a reorientation of the single particles within a nanocluster upon exposure of alternating magnetic field. However, the position for this discreteness is variable for the different samples mainly due to different size and size distribution of particles inside a nanocluster.

The specific absorption rate (SAR) of the magnetic fluid from heating curve was calculated using the SAR formula as mentioned in Eq. (8).

$$SAR = C_p \bullet \frac{\Delta T}{\Delta t} \bullet \frac{1}{\varphi_{magnetic}} \tag{8}$$

Where, C_p is the combined specific heat capacity of magnetic particles and carrier liquid, $\frac{\Delta T}{\Delta t}$ is the slope of the rise in temperature versus time graph and $\varphi_{magnetic}$ is the weight fraction of magnetic particles. The specific heat capacity of particles and carrier (water) was taken as 0.67 and 4.187 $Jg^{-1}K^{-1}$, respectively. The same fitting parameters was applied for all synthesized samples.

The heating response of all the samples is represented in Fig. 13 (b). The sample A55HT16 has the highest heating response of 360.9 ± 1.2 W/g_{Fe} as compared to other samples This is due to the small cluster size of 106.8 nm with the highest pore volume of 0.398 cm^3/g and the highest saturation magnetization of 79.08 Am^2/kg. It demonstrates that in the A55HT16 sample, the maximum heating response is observed at 360.9 ± 1.2 W/g_{mag}. The influence of hyperthermia on nanocluster sizes suggests that larger nanoclusters will result in a slower heating response.

The maximum SAR of 77.08 W/g_{Fe} for a monodispersed iron oxide magnetic nanocluster was obtained in the MFH study published by Ganesan et al. [12] at a frequency of 126 kHz and a field of 31.6 kA/m. Similar to this, Jamir et al. [18] conducted experiments using MFH at 336 kHz frequency, 14.92 kA/m magnetic field and 1 mg/mL concentration of Fe_3O_4 monodispersed magnetic nanoclusters coated with chitosan and dextran. Their results showed that the SAR for dextran-coated materials reduced from 233.28 W/g to 119.18 W/g as concentration increase from 1 to 3 mg/mL, while the SAR for chitosan-coated nanoclusters decreased from 161.15 to 114.31 W/g. Another experiment for the MFH study (f: 500 kHz; H: 37.4 kA/m; concentration: 1 mg/mL; time: 10 min) of different sizes of nanoclusters from 25 nm to 300 nm was performed by Jeong et al. [11].They observed that, as the size of nanoclusters increases, the SAR value decreases. Similarly, Herynek et al. [37] have reported the applicability of manganeze-zinc ferrite as an efficient and safe nanolabel for cell imaging and in vivo tracking.

4. Conclusion

We report the synthesis of monodispersed $Mn_{0.5}Zn_{0.5}Fe_2O_4$ magnetic nanoclusters with a controllable size using a hydrothermal method. The size of the nanoclusters was tuned by changing the reaction time from 5 to 24 h. The synthesized nanoclusters were characterized using XRD,

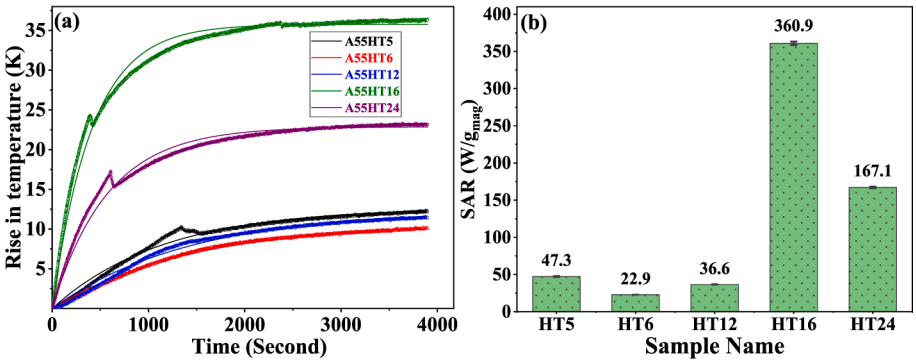

Fig. 13. (a) The plot of temperature versus time for $Mn_{0.5}Zn_{0.5}Fe_2O_4$ nanoflowers synthesized by hydrothermal route for different time at fixed parameters such as, 333 kHz frequency, 10 kA/m magnetic field and 1.7 mg/mL concentration (b) SAR variation for all samples.

FTIR, TGA, TEM, DLS, Zeta potential, U/SAXS, BET, and VSM. The XRD pattern confirms the pure FCC crystal structure of all the samples. The XRD results also confirm that the crystallinity of the particles increases as the reaction time increases. The coating of TMAOH on the surface was confirmed by FTIR and TGA. TEM indicates that magnetic nanoclusters are spherical nanoflowers and monodispersed in nature, with a tunable size range of 107 nm to 218 nm. The hydrodynamic size of nanoclusters from intensity distribution agrees well with the TEM results, and also no extra peak was found in the DLS results confirming that there is no aggregation of clusters present in the samples. The good colloidal stability of magnetic fluid was confirmed by zeta potential ($\zeta < -40$ mV). The U/SAXS results indicate that the system is an accumulation of small particles of ~ 7 nm forming a cluster of ~ 107–218 nm and entrapping some kind of polymer inside the cluster. All the samples are fitted with a model representing a core–shell structure with a core size comparable to that obtained from other techniques like TEM and DLS. Also, the size of the small particles inside the cluster is about 13–19 nm obtained from the XRD, whereas 19–24 nm is revealed from TEM measurement.

The adsorption–desorption isotherm plots measured using BET demonstrate that all the samples exhibit a H4 type of hysteresis loop, which indicates the mesoporous structure of the nanoflowers. The results also indicate that all the samples possess a high surface area and pore volume, confirming the porous structure of the samples. The maximum pore volume of 0.398 cm^3/g is observed in the A55HT16 sample.

The magnetic size is about 7.48 to 18.34 nm, again obtained from the core–shell model fitted with the magnetization data. The thickness of the shell contributes to paramagnetic susceptibility. The synthesized nanoclusters were further investigated for the induction heating experiment; results revealed that the maximum heating response was received in the A55HT16 sample with a SAR of 360.9 ± 1.2 W/g_{mag}. The results of the heating response show that as the density of the cluster and cluster size increase, the SAR value decreases. These magnetic nanoclusters have a porous structure that could be have an efficiency to load a drug inside the void, rendering their possible application in targeted drug delivery and magnetic fluid hyperthermia combined with chemotherapy.

CRediT authorship contribution statement

Hima Patel: Data curation, Formal analysis, Writing – original draft, Writing – review & editing, Investigation. **R.V. Upadhyay:** Formal analysis, Writing – review & editing, Validation, Visualization. **Kinnari Parekh:** Conceptualization, Formal analysis, Funding acquisition, Investigation, Methodology, Project administration, Resources, Supervision, Validation, Writing – review & editing. **Dennys Reis:** Data curation, Formal analysis, Writing – review & editing. **Cristiano L.P. Oliveira:** Formal analysis, Investigation, Resources, Validation, Visualization, Writing – review & editing. **A.M. Figueiredo Neto:** .

Declaration of competing interest

The authors declare that they have no known competing financial interests or personal relationships that could have appeared to influence the work reported in this paper.

Data availability

Data will be made available on request.

Acknowledgements

HP thanks the Government of Gujarat for financial support under the SHODH scheme (student reference no. 202001300004). KP thanks the GOI for providing grant no. SERB/CRG/2021/001587. KP also thanks FAPESP (grant # 2022/04512-5) for providing financial support to carry out the U/SAXS study at USP, Brazil. This study was partially supported by Brazil, the National Council for Scientific and Technological Development (CNPq–465259/2014-6), the Coordination for the Improvement of Higher Education Personnel (CAPES), the National Institute of Science and Technology Complex Fluids (INCT-Fcx), and the São Paulo Research Foundation (FAPESP–2014/50983-3), (FAPESP–2016/24531-3).

References

[1] C.M. Liebl, S. Kutschan, J. Dorfler, L. Kasmann, J. Hubner, Systematic review about complementary medical hyperthermia in oncology, Clin. Exp. Med. 22 (2022) 519–565, https://doi.org/10.1007/s10238-022-00846-9.
[2] R.E. Rosensweig, Heating magnetic fluid with alternating magnetic field, J. Magn. Magn. Mater. 252 (2002) 370–374, https://doi.org/10.1016/S0304-8853(02)00706-0.
[3] C. Munoz-Menendez, I. Conde-Leboran, D. Serantes, R. Chantrell, O. Chubykalofesenko, D. Baldomir, Distinguishing between heating power and hyperthermic cell-treatment efficacy in Magnetic Fluid Hyperthermia, Soft Matter 12 (43) (2016) 8815–8818, https://doi.org/10.1039/C6SM01910B.
[4] H. Gavilán, K. Simeonidis E. Myrovali, E. Mazarío, O. Chubykalo-Fesenko, R. W. Chantrell, L. Balcells, M. Angelakeris, M. Puerto Morales, and D. Serantes, How size, shape and assembly of magnetic nanoparticles give rise to different hyperthermia scenarios, Nanoscale, 13 (37) (2021) 15631–15646, https://doi.org/10.1039/D1NR03484G.
[5] X. Liu, Q. Hu, Z. Fang, Q. Wu, Q. Xie, Carboxyl Enriched Monodisperse Porous Fe_3O_4 Nanoparticles with Extraordinary Sustained-Release Property, Langmuir 25 (13) (2009) 7244–7248, https://doi.org/10.1021/la901407d.
[6] S.P. Damodaran, Mesoporous magnetite nanoclusters as efficient nanocarriers for paclitaxel delivery, Chem. Sel. 5 (2020) 9261–9268, https://doi.org/10.1002/slct.202001102.
[7] Y. Liu, C. Li, H. Zhang, X. Fan, Y. Liu, and Q. Zhang, One-pot hydrothermal synthesis of highly monodisperse water-dispersible hollow magnetic microspheres and construction of photonic crystals, Chem. Eng. J., 259 (2015) 779–786, https://doi.org/ 10.1016/j.cej.2014.08.051.
[8] J. Kim, V.T. Tran, S. oh, C,S. Kim, J.C. Hong, S. Kim, Y.S. Joo, S. Mun, M.H. Kim, J. W. Jung, J. Lee, Y.S. Kang, J.W. Koo, and J. Lee, Scalable Solvothermal Synthesis of Superparamagnetic Fe_3O_4 Nanoclusters for Bioseparation and Theranostic Probes, ACS Appl. Mater. Interfaces, 10 (49) (2018) 41935–41946, https://doi.org/10.1021/acsami.8b14156.
[9] G.C. Hermosa, W.C. Chen, H.S. Wu, C.S. Liao, Y.M. Sun, S.F. Wang, Y. Chen, A. C. Sun, Investigations of the effective parameters on the synthesis of monodispersed magnetic Fe_3O_4 by solvothermal method for biomedical applications, AIP Adv. 10 (1) (2020), 015234, https://doi.org/10.1063/1.5130063.
[10] T. Leshuk, H. Krishnakumar, F. Gu, Size-Tunable Fe_3O_4 Spherical Nanoclusters Through a One-Pot Hydrothermal Synthesis, J. Nanosci. Nanotechnol. 15 (7) (2015) 5378–5383, https://doi.org/10.1166/jnn.2015.9003.
[11] M. Jeong, S. Lee, D.Y. Song, S. Kang, T.H. Shin, J.S. Choi, Hyperthermia Effect of Nanoclusters Governed by Interparticle Crystalline Structures, ACS Omega 6 (46) (2021) 31161–31167, https://doi.org/10.1021/acsomega.1c04632.
[12] V. Ganesan, B.B. Lahiri, C. Louis, J. Philip, S.P. Damodaran, Size-controlled synthesis of superparamagnetic magnetite nanoclusters for heat generation in an alternating magnetic field, J. Mol. Liq., 281 (2019) 315–323, https://doi.org/10.1016/j.molliq.2019.02.095.
[13] Y. Chen, J. Zhang, Z. Wang, Z. Zhou, Solvothermal synthesis of size-controlled monodispersed superparamagnetic iron oxide nanoparticles, Appl. Sci. 9 (23) (2019) 5157, https://doi.org/10.3390/app9235157.
[14] W. Wang, B. Tang, B. Ju, S. Zhang, Size-controlled synthesis of water-dispersible superparamagnetic Fe_3O_4 nanoclusters and their magnetic responsiveness, RSC Adv. 5 (2015) 75292–75299, https://doi.org/10.1039/C5RA14354C.
[15] W. Wang, B. Tang, S. Wu, Z. Gao, B. Ju, X. Teng, S. Zhang, Controllable 5-sulfosalicylic acid assisted solvothermal synthesis of monodispersed superparamagnetic Fe_3O_4 nanoclusters with tunable size, J. Magn. Magn. Mater. 423 (2017) 111–117, https://doi.org/10.1016/j.jmmm.2016.09.089.
[16] H. Deng, X. Li, Q. Peng, X. Wang, J. Chen, Y. Li, Monodisperse magnetic single-crystal ferrite microspheres, Angew. Chem. Int. Ed. 44 (18) (2005) 2782–2785, https://doi.org/10.1002/anie.200462551.
[17] B. Zou, Y. Liu, Y. Wang, Facile Synthesis of Highly Water-Dispersible and Monodispersed Fe_3O_4 Hollow Microspheres and Their Application in Water Treatment, RSC Adv. 3 (2013) 23327–23334, https://doi.org/10.1039/C3RA42716A.
[18] M. Jamir, R. Islam, L.M. Pandey, J.P. Borah, Effect of surface functionalization on the heating efficiency of magnetite nanoclusters for hyperthermia application, J. Alloy. Compd. 854 (2021), 157248, https://doi.org/10.1016/j.jallcom.2020.157248.
[19] S. Chaleawlert-umpon, N. Pimpha, Morphology-controlled magnetite nanoclusters via polyethyleneimine-mediated solvothermal process, Mater. Chem. Phys. 135 (1) (2012) 1–5, https://doi.org/10.1016/j.matchemphys.2012.03.111.
[20] Q. Zhang, M. Zhu, Q. Zhang, Y. Li, H. Wang, Fabrication and magnetic property analysis of monodisperse manganese-zinc ferrite nanospheres, J. Magn. Magn. Mater. 321 (19) (2009) 3203–3206, https://doi.org/10.1016/j.jmmm.2009.05.049.

[21] G. Ashiotis, A. Deschildre, Z. Nawaz, J.P. Wright, D. Karkoulis, F.E. Picca, J. Kieffer, The fast azimuthal integration Python library : pyFAI research papers, J. Appl. Cryst. 48 (2015) 510–519, https://doi.org/10.1107/S1600576715004306.
[22] E.B. Knudsen, H.O. Sørensen, J.P. Wright, G. Goret, J. Kieffer, FabIO : easy access to two-dimensional X-ray detector images in Python, J. Appl. Cryst. 46 (2013) 537–539, https://doi.org/10.1107/S0021889813000150.
[23] A.I. Saville, A. Creuziger, E.B. Mitchell, S.C. Vogel, J.T. Benzing, J. Klemm-Toole, K.D. Clarke, A.J. Clarke, MAUD Rietveld Refinement Software for Neutron Diffraction Texture Studies of Single- and Dual-Phase Materials, Integr. Mater. Manuf. Innov. 10 (2021) 461–487, https://doi.org/10.1007/s40192-021-00224-5.
[24] K. Parekh, R.V. Upadhyay, L. Belova, K.V. Rao, Ternary monodispersed $Mn_{0.5}Zn_{0.5}Fe_2O_4$ ferrite nanoparticles: Preparation and magnetic characterization, Nanotechnology, 17 (24) (2006) 5970–5975, https://doi.org/ 10.1088/0957-4484/17/24/011.
[25] A. Ouasri, A. Rhandour, M.C. Dhamelincourt, P. Dhamelincourt, A. Mazzah, Vibrational study of (CH3)4NSbCl6 and [(CH3)4N]2SiF6, Spectrochim. Acta Part A 58 (2002) 2779–2788, https://doi.org/10.1016/s1386-1425(02)00019-7.
[26] M. Deepty, C.H. Srinivas, E.R. Kumar, N.K. Mohan, C.L. Prajapat, T.V.C. Rao, S. S. Meena, A.K. Verma, D.L. Sastry, XRD, EDX, FTIR and ESR spectroscopic studies of co-precipitated Mn–substituted Zn–ferrite nanoparticles, Ceram. Int. 45 (6) (2019) 8037–8044, https://doi.org/10.1016/j.ceramint.2019.01.029.
[27] F. Kooli, F. Mizukami, Y. Kiyozumi, Y. Akiyama, Hydrothermal conversion of Na-magadiite to a new silicate layered structure in a TMAOH-water-1,4-dioxane system, J. Mater. Chem. 11 (7) (2001) 1946–1950, https://doi.org/10.1039/b101015h.
[28] P. Bender, J. Fock, C. Frandsen, M.F. Hansen, C. Balceris, F. Ludwig, O. Posth, E. Wetterskog, L.K. Bogat, P. Southern, W. Szczerba, L. Zeng, K. Witte, C. Gruttner, F. Westphal, D. Honecker, D. Gonzalez-Alonso, L.F. Barquin, C. Johansson, Relating Magnetic Properties and High Hyperthermia Performance of Iron Oxide Nanoflowers, J. Phys. Chem. C 122 (5) (2018) 3068–3077, https://doi.org/10.1021/acs.jpcc.7b11255.
[29] C. L. P. Oliveira, Investigating Macromolecular Complexes in Solution by Small Angle X-Ray Scattering, in *Current Trends in X-Ray Crystallography, edited by Dr. Annamalai Chandrasekaran*, D. A. Chandrasekaran, Ed. 2011, pp. 367–392.
[30] O.R. Santos, D. Reis, A.G. Oliveira-filho, C.L.P. Oliveira, A.M.F. Neto, Structure and local order of lyotropic cholesteric calamitic phases : The effect of the chiral molecule, J. Mol. Liq. 349 (2022), 118097, https://doi.org/10.1016/j.molliq.2021.118097.
[31] P. Debye, Molecular-weight determination by light scattering, J. Phys. Colloid Chem. 51 (1) (1947) 18–32, https://doi.org/10.1021/j150451a002.
[32] J.S. Pedersen, C. Riekel, Resolution Function and Flux at the Sample for Small-Angle X-ray Scattering Calculated in Position-Angle-Wavelength Space, J. Appl. Cryst. 24 (1991) 893–909, https://doi.org/10.1107/s0021889891003692.
[33] D.X. Chen, A. Sanchez, E. Taboada, A. Roig, N. Sun, H.C. Gu, Size determination of superparamagnetic nanoparticles from magnetization curve, J. Appl. Phys. 105 (083924) (2009), https://doi.org/10.1063/1.3117512.
[34] J. Smit and W. H. P. J, *Ferrites*. Philips Technical Library pg.158, 1959.
[35] R. Hergt, S. Dutz, Magnetic particle hyperthermia biophysical limitations of a visionary tumour therapy, J. Magn. Magn. Mater. 311 (1) (2007) 187–192, https://doi.org/10.1016/j.jmmm.2006.10.1156.
[36] R.R. Wildeboer, P. Southern, Q.A. Pankhurst, On the reliable measurement of specific absorption rates and intrinsic loss parameters in magnetic hyperthermia materials, J. Phys. D Appl. Phys. 47 (49) (2014), 495003, https://doi.org/10.1088/0022-3727/47/49/495003.
[37] V. Herynek, K. Turnovcová, A. Gálisová, O. Kaman, D. Marekova, J. Koktan, M. Vosmanska, L. Kosinova, P. Jendelova, Manganese-Zinc Ferrites : Safe and Efficient Nanolabels for Cell Imaging and Tracking In Vivo, Chem. Open 8 (2019) 1–12, https://doi.org/10.1002/open.201800261.